ADVANCED ENGINEERING MATERIALS
www.aem-journal.com



# The Electroless Monolayer and Duplex Ni–B and Ni–P Coatings for 316L Stainless Steel in Synergistic Combination of Mechanical (Wear) and Chemical (Corrosion) Processes

*Ferda Mindivan,* Harun Mindivan, and Ali Bayram*

**Conventional processes are performed to improve the low hardness and low wear resistance properties of 316L steel, but these processes generally decrease the corrosion resistance. Electroless nickel alloy coatings provide a hard, wear-resistant, and corrosion-resistant surface. Thus, the present study aims to investigate the wear, corrosion, and tribocorrosion behaviors of monolayer and duplex coatings with nickel–boron (Ni–B) and nickel–phospore (Ni–P) on 316L steel in comparison with 316L steel in dry sliding and 0.9 wt% NaCl solution environments. It is determined that the coatings have a mixture of crystal and amorphous structures, the interfaces on the 316L are uniform, and the compatibility between the layers is good. The Ni–B, Ni–P/Ni–B, and Ni–B/Ni–P coatings are 2.3, 2.06, and 1.6 times as hard as the 316L, respectively. The wear rates of Ni–B, Ni–P/Ni–B, and Ni–B/Ni–P coatings show decrease by 99.3%, 92.5%, and 99.1% in the dry-sliding condition and by 98.5%, 30.1%, and 19.1% in the tribocorrosion condition compared with that of 316L, respectively. It is observed that the monolayer Ni–B coating exhibits superior hardness, a higher contact angle, low electrical conductivity, and better tribological performance in both dry sliding and tribocorrosion conditions compared to the 316L and duplex coatings.**

## 1. Introduction

Wear and corrosion are old and well-known problems in many engineering applications. Therefore, steelmakers used various methods to improve both the wear and corrosion properties of steel under service conditions. It is an expensive method to manufacture the entire part from high wear- and corrosion-resistant materials. Wear and corrosion are surface damages; therefore, a suitable surface modification technique extends the service life of steels with both low cost and ease of mass production.[1] AISI 316L austenitic stainless steels exhibit excellent corrosion resistance with their austenitic microstructure and chromium oxide film layer on their surfaces in many aqueous and atmospheric environments. Because of these characteristics, they were widely used in a variety of industries, including food processing equipment (boiling pans, mashed tomato tanks, milk transport materials, oven parts), household appliances (forks, spoons), aerospace (aircraft exhaust chimneys, jet engine parts, pump parts), and chemical industry (pressurized containers), military applications, automotive industry, turbine blades, heat exchangers, railway cars, antennas, cold vessels, rain gutters, marine applications, biomedical applications (surgical implantology and surgical instruments), nuclear power plants (construction of primary circuit components), and important structural materials for indoor components. Stainless steels are known for their good corrosion resistance, but corrosion resistance may decrease in aggressive environments with sulfur, chloride, or other anions compared to homogeneous corrosion against local corrosive attacks such as stress corrosion, intergranular corrosion, and pitting corrosion. In addition, its usage areas are limited due to low hardness, poor wear and fatigue resistance, and a high "density/mechanical properties" ratio. As a result, various surface treatments can broaden the applications of 316L-type stainless steels.[2,3] In recent years, surface modification processes have been carried out on steel surfaces by electroless coating processes. Electroless coating technology, since its inception by Brenner and Riddell (1946), has been an autocatalytic process with a

F. Mindivan
Faculty of Engineering
Department of Bioengineering
Bilecik Seyh Edebali University
Bilecik 11100, Turkey
E-mail: ferda.mindivan@bilecik.edu.tr

H. Mindivan
Faculty of Engineering
Department of Mechanical Engineering
Bilecik Seyh Edebali University
Bilecik 11100, Turkey

A. Bayram
Faculty of Engineering and Architecture
Department of Mechanical Engineering
Uludağ University
Görükle-Bursa 16059, Turkey

The ORCID identification number(s) for the author(s) of this article can be found under https://doi.org/10.1002/adem.202201501.

**DOI: 10.1002/adem.202201501**

 

controlled chemical reduction reaction.[1] Electrodes are not used in such coatings; metal deposition takes place as a result of an autocatalytic reaction after nucleation begins on the metal surface. In addition, the electroless coating method is used for coating not only flat surfaces but also complex-shaped parts and even particles, independent of the shape and size of the substrate material.[4] Electroless coatings have unique physicochemical and mechanical properties that make them usable, such as homogeneity, excellent corrosion resistance, wear resistance, solderability, high hardness, amorphous microcrystalline deposition, and a low friction coefficient. Most applications of electroless coating in the electronics, oil and gas, chemical, and automotive industries are based on wear and corrosion resistance. And also, the luminescence property of electroless coatings enables them to be used in the defense and aircraft industries.[1] Electroless nickel coatings have the greatest commercial importance among electroless coatings and are the most frequently used coating type to produce phosphorus/boron (P/B) alloy coatings of varying compositions. Generally, the coating composition ranges from 2% to 14% by weight for phosphorus and from 0.1% to 10% by weight for boron. This variation affects the coating properties of the alloy content. Nickel–phosphorus (Ni–P) coatings are uniform, hard, brittle, lubricious, easily solderable, and highly wear-resistant. The combination of these properties makes the coatings suitable for many demanding applications and allows them to be used as substitutes for alloys. The properties of Ni–B coating are mostly similar to those of Ni–P coating. The hardness of the heat-treated Ni–B alloy is very high compared to hard chromium. It has excellent wear resistance. Ni–B coatings are more costly than Ni–P, but they have low corrosion resistance. Although Ni–P is widely used commercially, Ni–B seems to be an alternative to chrome coating with its superior hardness.[5] Electroless coatings can be applied to steel, stainless steel, magnesium, and aluminum alloys.[6–9] Zhang et al.[10] developed 35 mm-thick electroless duplex Ni–P/Ni–B coatings on AZ91D magnesium alloy and investigated the morphological, microhardness, and corrosion resistance properties of these coatings. It was reported that Ni–P/Ni–B coatings significantly improved the hardness and corrosion resistance of magnesium alloy substrates. AZ91D magnesium alloy was coated with an electroless duplex Ni–P/Ni–B coating in another study by Zhang et al.[11] They reported that Ni–B acts as the cathodic protective and sealing layer of the outer layer. And also, Ni–P inner layer has been seriously inhibited chlorine ion attack in the NaCl solution. Vitry et al.[9a] obtained duplex Ni–P/Ni–B coatings on 2024 aluminum alloy and investigated the wear and corrosion resistance of these coatings. They reported that the coated samples had good corrosion resistance before heat treatment and had a corrosion potential close to −250 mV. Narayanan et al.[12] formed electroless Ni–P/Ni–B duplex coatings on mild steel, and the hardness, wear resistance, and corrosion resistance of these coatings were investigated. Between the two types of duplex coatings examined, it was determined that duplex coatings with Ni–B coating as the outer layer had higher hardness and wear resistance, while those with Ni–P coating as the outer layer offered better corrosion resistance. The wear mechanism of duplex coatings is defined as "adhesive wear." Baibordi et al.[13] investigated the tribological properties of electroless Ni–P and duplex Ni–P/Ni–B electroless coatings on CK45 steel. As a result, they reported that the hardness and wear resistance of the duplex coating increased compared to the monolayer Ni–P coating. Vitry et al.[14] determined the structural and morphological characteristics of electroless monolayer, duplex Ni–B/Ni–P, and Ni–P/Ni–B coatings on the surface of St-37 steel at the same coating thickness. They analyzed that the interface of Ni–P as the outer layer was completely smooth in duplex coating, but a rough interface of Ni–B as the outer layer was also observed. Electroless duplex Ni–P/Ni–B and monolayer Ni–B coatings on a 410 martensitic stainless-steel substrate were applied by Tohidi et al.[7] The results showed that the hardness value and wear resistance of the duplex coating with high P content increased compared to the monolayer coating, but the surface roughness decreased. They reported that the hardness values of duplex coatings with medium and low P contents were lower than those of the monolayer Ni–B coating, and the weight losses were also higher after the wear test. Zhao et al.[15] prepared Ni–P–$TiO_2$ nanocomposite coatings on 316L stainless steel and investigated their antibacterial properties. Bülbül et al.[3] characterized the structural, tribological, and corrosion properties of the electroless Ni–B coating on AISI 316L stainless steel. The results of this study showed that the monolayer coating could not only improve the hardness and wear resistance of 316L stainless steel but also provide cathodic protection with the original properties of this material. As can be seen from the results of all these studies, it has been determined that Ni-based alloy coatings have significant effects on the corrosion and wear properties of the substrate material. Specially, tribological properties,[16–18] corrosion behaviors,[19,20] and oxidation resistance[21] of electroless monolayer or duplex Ni, Ni–B, and Ni–P coatings were investigated with recent studies. In this study, in addition to the literature, monolayer Ni–B and duplex Ni–P/Ni–B and Ni–B/Ni–P coatings were applied to AISI 316L stainless steel to improve its low hardness and poor wear resistance. There is no report in the literature on 316L duplex coatings and their dry sliding, corrosion, and tribocorrosion properties. The motivation for this study was the scarcity of studies examining the effect of electroless coatings on 316L and the combined effect of wear–corrosion. The combination of wear and corrosion mostly affects the life of the material in the working environment.

## 2. Experimental Section

### 2.1. Materials and Electroless Coating

AISI 316L disc-shaped samples with 18 mm diameter and 2 mm thickness were used as the substrate for the preparation of electroless coating. Chemical composition of the substrate is given in **Table 1**.

Before coating, all samples were grinded with 240, 400, 600, 800, 1000, and 1200 grit SiC abrasive paper, respectively; cleaned in alcohol and mechanically polished with a fine grade $Al_2O_3$ paste. A commercial product, SurTec 179, that is a high-alkaline cleaner

**Table 1.** Chemical composition of the AISI 316L.

| Element | C | Cr | Mo | Ni | Si | Mn | P | S | Fe |
|---|---|---|---|---|---|---|---|---|---|
| wt% | 0.021 | 16.82 | 2.44 | 11.5 | 0.406 | 1.50 | 0.0338 | 0.0478 | 66.19 |

 

to obtain a smooth and homogeneous coating layer was used for surface treatment of samples. After polishing, the samples were degreased with SurTec 179 (7–8 vol%) for 5 min at 60 °C. After that, the surface of samples was activated by immersing them in 20% $H_2SO_4$ solution for 1 min and washed in distilled water. 316L stainless steel samples were electrolytically coated with Ni using direct current before all electroless coating processes. The aim of the electrolytical nickel coating was to enhance the adhesion between electroless Ni–P and Ni–B coatings and 316L.[22] This process was abbreviated as DC. In the electrolytic Ni coating process, 316L with 18 mm diameter and 2 mm thickness as cathode material and Ni plates in the size of 30 mm × 50 mm × 2 mm were used as anode material. The coatings were prepared under direct current conditions by a current density of 5 $dm^{-2}$ from a Watts-type bath. Composition and coating parameters for electrolytic Ni coating are given in **Table 2**.

Electrolytic Ni-coated samples were coated with electroless Ni–B monolayer and electroless duplex Ni–B/Ni–P, Ni–P/Ni–B coatings, respectively. Composition and coating parameters for electroless monolayer Ni–B coating are given in **Table 3**.

The electroless monolayer Ni–B coating was carried out using sodium borohydride ($NaBH_4$) as a reducer, nickel chloride hexahydrate ($NiCl_2.6H_2O$) as a nickel source, ethylenediamine ($C_2H_8N_2$) as a complexing agent, sodium hydroxide (NaOH) as a pH adjuster, and lead nitrate ($Pb(NO_3)_2$) as a stabilizer. The coating bath took place at 95 ± 1 °C in a thermostable cell with a volume of 250 mL, under constant mechanical agitation (250 rpm), and pH (13.5) for 60 min. For the coatings of the duplex system, the electrolytic Ni-coated 316L surface was first immersed in electroless Ni–B bath given in Table 3 for the inner layer of deposition. For the outer layer of coating, the Ni–B-coated samples were dipped in an electroless Ni–P solution. Electroless Ni–P solution was prepared from 5 g $L^{-1}$ nickel, 40 g $L^{-1}$ sodium hypophosphite ($NaH_2PO_2$), and a commercial powder (DURNI-COAT DNC 520-9) containing appropriate amounts of additives and stabilizers. The same deposition conditions were used with the Ni–B coating. The Ni–B/Ni–P duplex coatings were removed from the coating bath after 60 min of last deposition, washed in deionized water, and dried. In a similar manner, duplex Ni–P/Ni–B (Ni–P as an inner layer and Ni–B as the outer layer of deposition) system was deposited.[23] The images of 316L and electroless coatings are given in **Figure 1**.

**Table 2.** Composition and coating parameters for electrolytic Ni coating.

| Composition | – |
|---|---|
| $NiSO_4.6H_2O$ | 300 g $L^{-1}$ |
| $NiCl_2.6H_2O$ | 50 g $L^{-1}$ |
| $H_3BO_3$ | 40 g $L^{-1}$ |
| SDS (sodium dodecyl sulfate) | 0.1 g $L^{-1}$ |
| Coating parameters | |
| Temperature | 50 ± 5 °C |
| pH | 4 ± 2 |
| Current density | 5 A $dm^{-2}$ |
| Current | DC |
| Magnetic stirring | 30 min |
| Ultrasonic mixing | 30 min |
| Anode | Ni |
| Cathode | 316L |

**Table 3.** Composition and coating parameters for electroless monolayer Ni–B coating.

| Composition | – |
|---|---|
| $NaBH_4$ | 1.2 g $L^{-1}$ |
| $NiCl_2.6H_2O$ | 10 g $L^{-1}$ |
| $C_2H_8N_2$ | 90 g $L^{-1}$ |
| NaOH | 90 g $L^{-1}$ |
| $Pb(NO_3)_2$ | 0.0145 g $L^{-1}$ |
| Coating parameters | – |
| Temperature | 95 °C |
| pH | 13.5 |
| Time | 60 min |

## 2.2. Characterization

The scanning electron microscope (SEM) (Zeiss, Supra 40VP) with energy-dispersive X-Ray spectrometry (EDS) and Nikon Eclipse LV150 model optical metal microscope (OM) were used to observe coating morphology and surface morphology of the coating after dry sliding wear, corrosion, and tribocorrosion tests. The wettability of the coatings was tested using Biolin Scientific, Theta Lite contact angle test device at room temperature. The electrical conductivity of the samples was measured by using a SIGNATONE programmable automatic KEITHLEY meter with a four-point probe. Phase analysis of coatings was examined by X-ray diffraction (XRD-PAN analytical Empyrean) using Cu Kα radiation (λ = 1.5404 Å) in the 2$\theta$° range of 10°–90°.

Microhardness measurements of the coatings were measured using Vickers method with a load of 50 g where the reported values were in the average of five measurements.

Dry sliding wear tests of the coatings were carried out on a reciprocating wear tester using alumina ($Al_2O_3$) balls. $Al_2O_3$ ball was chosen as counterface material due to its high hardness, high wear resistance, chemical inertness, and electrical insulating properties. Other conditions of wear test are given in **Table 4**. The coefficient of friction (COF) was recorded automatically by

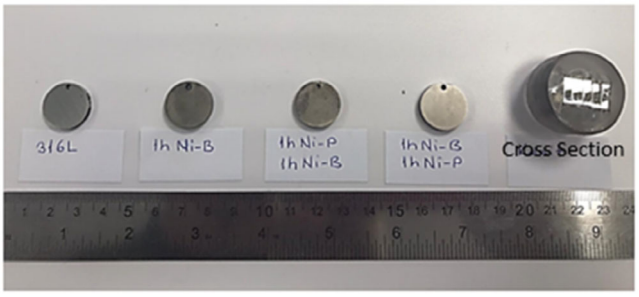


**Figure 1.** The images of 316L and electroless coatings.

**Table 4.** Dry sliding conditions.

| | |
|---|---|
| Load [N] | 5 |
| Wear track length [mm] | 11 |
| Sliding velocity [cm $s^{-1}$] | 1.9 |
| Sliding time [s] | 2880 |
| Sliding distance [m] | 57.5 |
| Humidity [%] | $30 \pm 5$ |
| Temperature [°C] | $25 \pm 5$ |

the loadcell mounted in the tester. After the wear tests, the profile of the wear tracks was measured with the Mitutoyo Surtest SJ-400 profilometer. Three wear track topographic profiles were produced for each sample. In addition, the surface roughness of the coatings was measured with the same profile instrument. $R_a$: arithmetic average height, $R_q$: root mean square roughness, $R_y$: largest peak to valley height, and $R_z$: ten-point height (μm) obtained from the profiles.

In electrolytic corrosion tests, ≈0.2 $cm^2$ surface area of the 316L and electroless coatings that working electrode were contacted with the solution. 0.9 wt% NaCl solution was used as the test solution. A Gamry model PC4/300 mA potentiostat/galvonostat test unit was used in the electrolytic corrosion test by a computer with DC 105 Corrosion analysis software. Before potentiodynamic polarization measurements, an initial delay of 1800 s was operated in order to determine the open circuit potential (OCP) between reference and working electrodes. Potentiodynamic polarization curves were generated by scanning the potential from cathodic to anodic direction at a scan rate of 1 mV $s^{-1}$, starting from −0.6 up to −0.1 V. The corrosion potential ($E_{corr}$) and corrosion current density ($I_{corr}$) were measured using the Tafel extrapolation method. Finally, the surface images of the 316L and the corroded coatings were investigated using an SEM for their corrosion morphology.

The tribocorrosion tests of the 316L and electroless coatings were conducted in the 25 mL of the same electrolyte that used in corrosion tests by using a reciprocating wear tester coupled with three-electrode electrochemical cell. Reciprocating sliding wear tests were applied in a reciprocating mode with a 1.9 cm $s^{-1}$ sliding rate under 5 N applied load for 45 min at OCP conditions. The OCP was evaluated before, during, and after sliding where the sliding action started after reaching the stable OCP values for three tests. The counterface material was an $Al_2O_3$ ball with 10 mm diameter. The $Al_2O_3$ holder was made of a polymeric material to hinder the corrosion effects. During the test, surface with an area of 2.5 $cm^2$ was contacted to the corrosive electrolyte. After tribocorrosion tests, the worn surfaces of the tested samples and corresponding $Al_2O_3$ balls were investigated by the SEM and OM, respectively.

## 3. Results and Discussions

### 3.1. Coating Morphology

OM (a,b) and SEM (c,d) surface images at different magnifications, and EDS surface mapping analysis (e) of an electroless monolayer Ni–B coating are shown in **Figure 2**a–e. The dense, compact, and homogeneous structure of many cauliflower-like spherical grains of monolayer Ni–B coating is depicted in Figure 2a–d. And also, the high-magnification OM and SEM surface images in Figure 2b–d were examined; no defects were determined in the grain boundaries. The cauliflower-like nodular structure of the monolayer Ni–B coating was consistent with the literature.[24,25] A combination of many spherical grains created the rough surface structure, and this structure decreased the surface contact area (Figure 14) and increased the wear resistance (Table 7) of the coatings. The EDS mapping analysis of the electroless Ni–B coating in Figure 2e-(1-3)) showed the presence of nickel density with red dots (Figure 2e-1); oxygen (Figure 2e-2) and boron (Figure 2e-3) elements were also clearly seen with blue and green dots, respectively.

**Figure 3**a–e showed OM (a,b) and SEM (c,d) surface images, and EDS surface mapping analysis (e-(1-3)) of an electroless duplex Ni–P/Ni–B coating. OM and SEM images demonstrated a typical cauliflower-like structure without porosity and completely covered by the Ni–B in the outer layer in Figure 3a–d. The high-P content Ni–P layer on the inner surface of duplex coatings created this compact structure. Tohidi et al.[7] reported that the surface morphologies of high P content coatings (Ni 12.10% P) were more compact than electroless duplex Ni–P/Ni–B coatings with medium and low P content on 410 martensitic stainless steel. In this study, the distribution of nickel (Figure 3e-1, oxygen (Figure 3e-2, and boron elements (Figure 3e-3 was shown one by one by EDS mapping and the chemical compositions of electroless coatings obtained from EDS analysis are given in **Table 5**. The high P content (Table 5) of the coatings supported the compact structure in Figure 3. As can be seen from Figure 2 and 3, spherical nodules of varying sizes were formed in the duplex Ni–P/Ni–B coating, but the presence of more homogeneous nodules was observed in the monolayer Ni–B coating surface. The formation of smoother and more uniform grains revealed that the self-lubricating character of the monolayer Ni–B coating would be higher than that of the duplex coating. The positive effect of the uniform and smooth structure of the coating surface on the wear resistance was emphasized in the electroless duplex Ni–P/Ni–B coating studies on magnesium alloy by Zhang et al.[10]

The OM (a,b) and SEM (c,d) surface images at different magnifications and the EDS mapping analysis (e-(1-3)) of the electroless duplex Ni–B/Ni–P coating are given in **Figure 4**a,e. The surface morphology of the duplex coating is shown in Figure 4a,d, which fully covered the 316L substrate and showed typical spherical nodules with a uniform structure. The high density, nonporous, and smooth surface of the coating was compatible with the surface images of duplex Ni–B/Ni–P coating given in the literature .[8] In Figure 4e-(1-3), the presence of nickel, oxygen, and boron elements, represented by large amounts of red dots (Figure 4e-1), blue dots (Figure 4e-2), and small amounts of green dots (Figure 4e-3), was also clearly seen, respectively, by EDS mapping analysis.

### 3.2. Cross-Sectional Morphology of Coating

In order to determine the thickness and coating quality of the electroless coatings, the cross-sectional images were examined with OM, and the images are given in **Figure 5**a–f. The cross-sectional

 

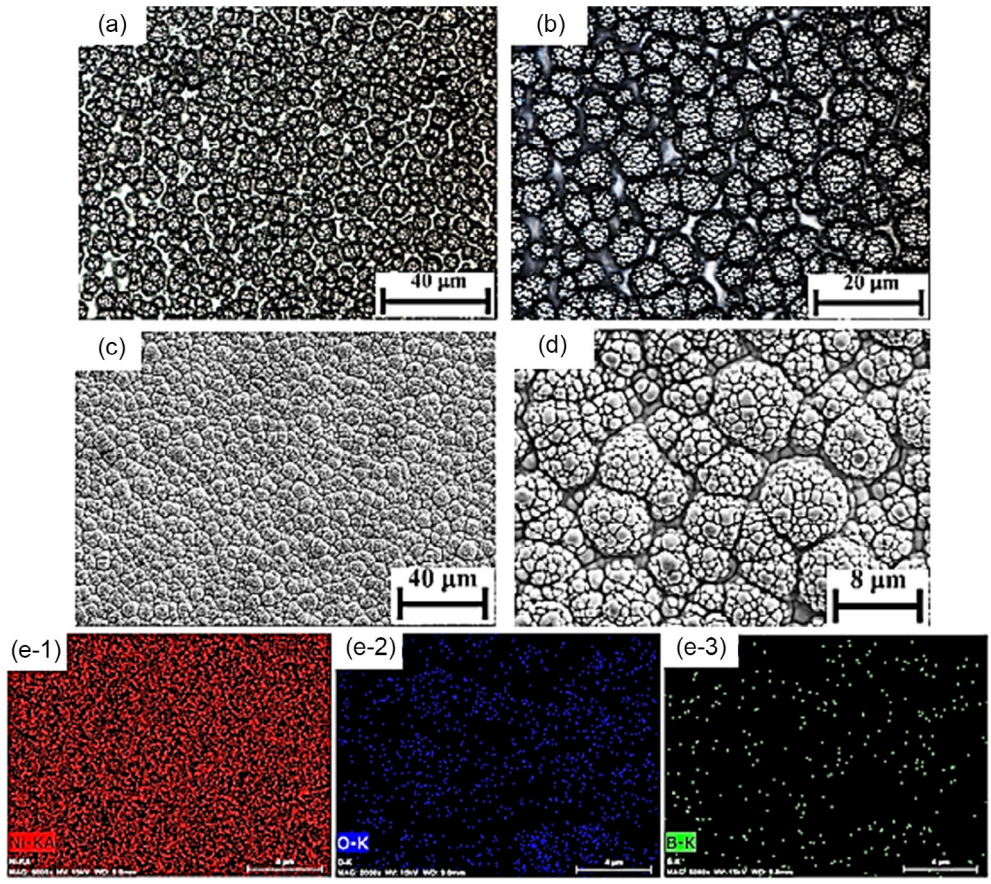


**Figure 2.** a,b) OM and c,d) SEM surface images, and e-(1-3) EDS surface mapping analysis of electroless monolayer Ni–B coating.

images of all coatings showed that the formed coatings were uniform and compact at the corners of the 316L substrate. It was determined that the monolayer Ni–B coating showed columnar growth on the DC coating, and the thickness of the DC was ≈67.1 μm while the value for the Ni–B layer was ≈10.87 μm (Figure 5a,b). As shown in Figure 5c,d, the electroless Ni–P/Ni–B duplex coatings of DC, Ni–P, and Ni–B layers thicknesses were ≈68.18, ≈18.67, and ≈7.89 μm, respectively. And also, in Figure 5e,f, the cross-sectional images of the Ni–B/Ni–P duplex coating showed that the DC layer thickness was 36.92 μm, the inner layer (Ni–B) was 12.47 μm, and the outer layer (Ni–P) was 11.26 μm. The columnar structure representing the Ni–B coating was clearly seen in Figure 5f.

### 3.3. XRD Analysis of Coating

The XRD patterns of 316L substrate, monolayer Ni–B, duplex Ni–P/Ni–B, and Ni–B/Ni–P coatings are shown in **Figure 6**, respectively. The XRD pattern of 316L exhibited three peaks at $2\theta^\circ = 43.5^\circ$, 50.7°, and 74.4°, which matched, respectively, to the (111), (200), and (220) of 316L stainless steel reflections, suggesting a crystalline structure.[26] The diffraction pattern of all the electroless coatings shown in Figure 6 showed that they consist of a mixture of amorphous and crystalline phases. Baskaran et al.,[27] Bülbül et al.,[3] and Czagány et al.[28] also observed the mixture structure of electroless coatings. Madah et al.,[24] Krishnaveni et al.,[29] and Vitry et al.[9a] indicated that electroless coatings were in an amorphous state with a broad diffraction peak at $2\theta^\circ = 40^\circ$–$50^\circ$. These results were similar to the other experimental result where the boron content was greater than 4.00 wt%.[9b] The amorphous–crystalline mixture structure of these coatings, which contain 4.00 wt% boron as shown in Table 5, was an expected result. Barman et al.[30] discovered a peak at nearly 53° in the XRD pattern of electroless Ni–B coatings, which was attributed to the presence of an amorphous and crystalline mixed-phase structure. They also stated that coatings with boron contents greater than 4% typically have an amorphous structure. Zhang et al.[31] reported that the Ni–P coatings had a characteristic peak of Ni near $2\theta^\circ = 44.6^\circ$ (111), and their structure was between crystalline and amorphous due to the phosphorus in the coating causing their highly disordered lattice structure. Rajabalizadeh et al.[19] showed the XRD analysis results of the Ni–P coating and observed the characteristic peak of Ni (111) at about 45°. In this study, the peaks at $2\theta^\circ = 44.8^\circ$ and $2\theta^\circ = 52.6^\circ$ that appeared in all diffractograms corresponded to the (111) plane of the characteristic peak of Ni and mixture structure, respectively.

### 3.4. Surface Roughness of Coatings

Surface roughness values of 316L and electroless coatings were compared in **Figure 7**. It was an expected result to have a smooth

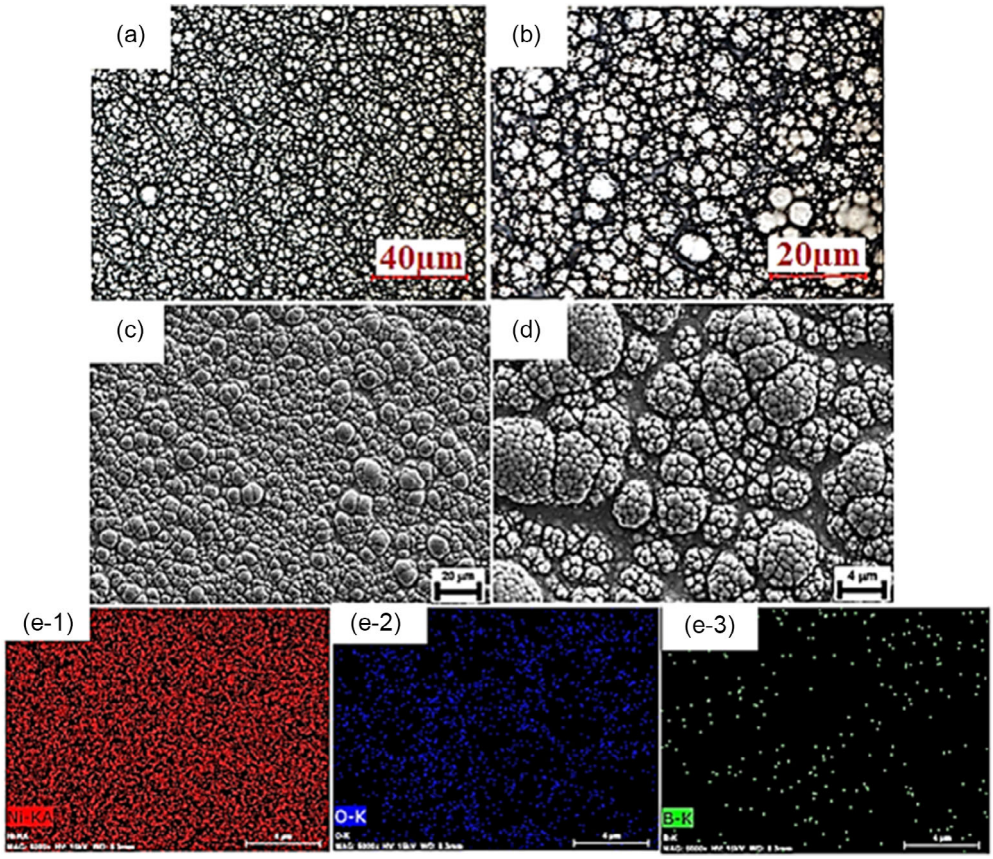


**Figure 3.** a,b) OM and c,d) SEM surface images, and e-(1-3) EDS surface mapping analysis of electroless duplex Ni–P/Ni–B coating.

**Table 5.** Chemical compositions of electroless coatings.

| Coating | Ni [wt%] | P [wt%] | B [wt%] |
|---|---|---|---|
| Ni–P | 83.3 | 11.6 | – |
| Ni–B | 96 | – | 4.0 |

surface on the polished 316L that had no surface treatment. According to Figure 7, the duplex Ni–B/Ni–P layer was less rough than the other layers. The surface roughness of the monolayer Ni–B coating was lower than the duplex Ni–P/Ni–B coating. The high roughness was caused by the morphology of the Ni–B top layer, which had many cauliflower-like spherical grains. It was determined that spherical grains of varying sizes were formed in the duplex Ni–P/Ni–B coating in Figure 3a–d and more homogeneous grains were formed in the microstructure of the monolayer Ni–B coating in Figure 2a–d. For this reason, the duplex Ni–P/Ni–B coating exhibited the highest surface roughness.

### 3.5. Microhardness Test

The microhardness values of 316L and the electroless coatings are given in **Table 6**. The monolayer Ni–B, duplex Ni–P/Ni–B, and Ni–B/Ni–P coatings were 2.3, 2.06, and 1.6 times as hard as the 316L, respectively. The high hardness could be attributed to the internal stress that was stored in the layers.[7] The microhardness values of the monolayer Ni–B and duplex Ni–P/Ni–B coatings were higher than those of the Ni–B/Ni–P coating (Table 6). The hardness results of this study were compatible with the hardness results of monolayer Ni–B, duplex Ni–P/Ni–B, and Ni–B/Ni–P coatings on different alloys reported in the literature. For example, Zhang et al.[8] reported that the microhardness value of the duplex Ni–B/Ni–P coating on AZ91D Mg alloy was 500 $HV_{0.01}$, the monolayer Ni–B coating was 650 $HV_{0.01}$, and the monolayer Ni–P coating was 400 $HV_{0.01}$. The hardness of the duplex Ni–P/Ni–B coating on 2024 aluminum alloy was 834 $HK_{0.05}$, which was determined by Vitry et al.[9a] and Bülbül et al.[3] showed that the monolayer Ni–B coating had a microhardness of 690 $HK_{0.01}$.

### 3.6. Dry Sliding Wear Test

**Figure 8** shows the friction coefficient profiles of the 316L and electroless coatings. The wear volumes and wear rates of the same samples are given in **Table 7**. As can be seen from Figure 8, the variation of the friction coefficients of the coatings appeared to be lower and had minor oscillations compared to 316L. The average friction coefficient of 316L was 0.91, but the average friction coefficient values of monolayer Ni–B, duplex Ni–P/Ni–B, and Ni–B/Ni–P coatings were found to be 0.67, 0.67, and 0.68, respectively. Mukhopadhyay et al.[32] discovered that

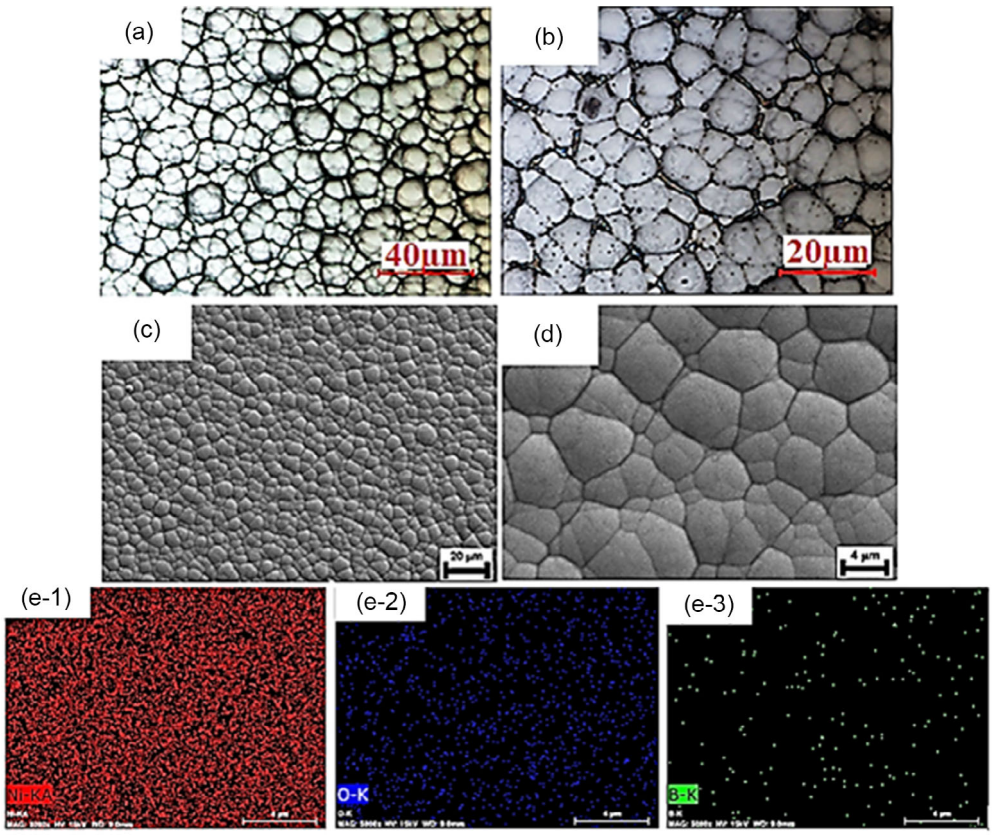


**Figure 4.** a,b) OM and c,d) SEM surface images, and e-(1-3) EDS surface mapping analysis of electroless duplex Ni–B/Ni–P coating.

Ni–B coatings had low friction coefficient values due to their high hardness and lower actual contact area; Nemane et al.[33] discovered that friction coefficient was related to the extent of wear at wear tracks in the form of spallation, cracks, and debris; and Jasim et al.[34] discovered that friction coefficient was related to materials removal from the surface and contact area between the surface and counterpart. In this study, the low coefficient of friction values of the coatings was visible from the SEM micrographs of wear tracks shown in **Figure 9**b,e,h,k. The oscillation in the friction coefficient was attributed to the large amount of wear debris on the worn surface of 316L (Figure 9b,e,h,k) and the lower contact area of the coatings due to the compact nodular surface morphology of the coatings (Figure 2, 3, and 4). The friction coefficient profile of the monolayer Ni–B coating had lower oscillation than that of duplex coatings. As can be seen from Table 7, a significant difference was observed between the wear volume and wear rate values of the substrate materials and electroless coatings. The wear rates of monolayer Ni–B, duplex Ni–P/Ni–B, and Ni–B/Ni–P coatings showed decrease by 99.3%, 92.5% and 99.1% in the dry-sliding condition compared with that of 316L, respectively. All results showed that the coatings significantly increased the wear resistance of 316L. The monolayer Ni–B coating had the most stable friction coefficient profile, the lowest wear volume and wear rate values than that of duplex coatings. This could be attributed to the compact structure with more homogeneous nodules (Figure 2) and higher hardness of monolayer Ni–B coating (Table 6).

Between the two types of duplex coatings, the coating with a Ni–B outer layer exhibited a higher specific wear rate. The SEM images of a worn surface and the OM surface images of counterface material in Figure 9a-I explained this unexpected result. At low magnification, the wear width of 316L was greater than that of all other coatings (Figure 9a). From the high-magnification images of the 316L, it could be seen that the severe adhesive wear by plastic deformation tracks was dominant (Figure 9b). A large amount of wear debris was seen over the entire worn surface during the severe wear process due to the low hardness of 316L (Table 6). Similar images were reported using different counterface materials by Saravanan et al.[35] and Li et al.[36] It is known that wear debris increases the wear rate during sliding.[36] The OM image of the counterface material showed that a large amount of wear debris had transferred onto the $Al_2O_3$ ball surface (Figure 9c). Wear debris was a possible cause of the higher wear rate, adhesive wear mechanisms, and high oscillations on the friction coefficient profile of the 316L substrate (Figure 8 and Table 7). The low-magnification SEM image of the monolayer Ni–B coating represented that the wear width was significantly reduced compared to the wear width of 316L (Figure 9d). The high-magnification SEM image revealed microcracks (Figure 9e). Furthermore, a worn surface image that was flat and smooth clearly demonstrated that this coating significantly improved the wear resistance of 316L. Tohidi et al.[7] reported the wear properties of monolayer Ni–B on 410 stainless steels. The worn surface of this coating had small pits, and the

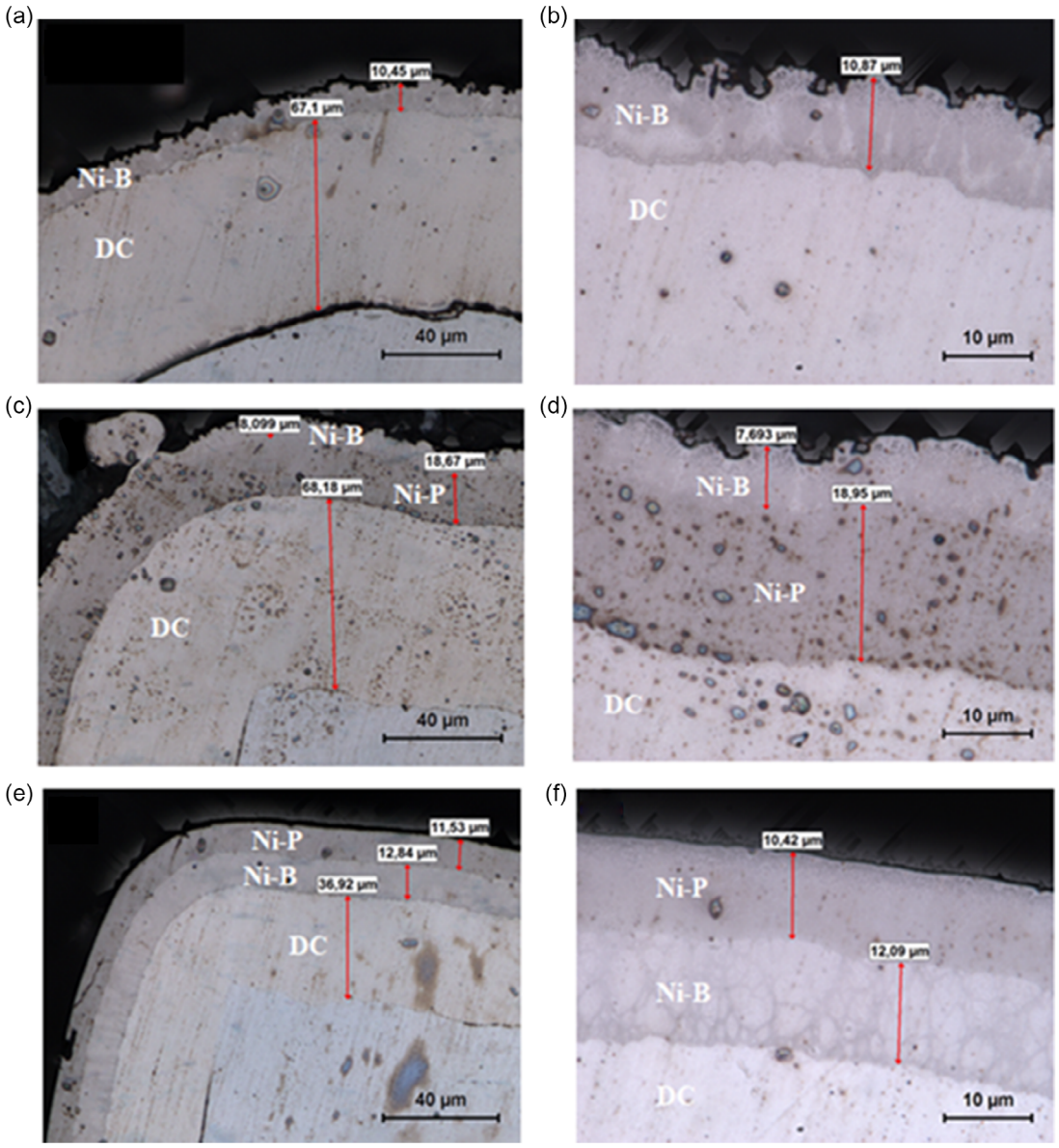


**Figure 5.** The cross-sectional images of electroless monolayer a,b) Ni–B, c,d) duplex Ni–P/Ni–B, and e,f) duplex Ni–B/Ni–P coatings.

wear mechanism was adhesive wear. Madah et al.[24] found that during the wear test on medium carbon steel with Ni–B coating, the asperity on the surface was broken due to the high hardness of the counterface $Al_2O_3$ ball. They reported that adhesive wear tracks were seen on the worn surface as a result of plastic deformation. But in this study, no adhesive wear tracks were observed except for the cracks on the surface. It was thought that the brown tracks on the counterface material were caused by nickel oxide formed due to high contact stresses and friction heat between the $Al_2O_3$ ball and the Ni–B coating surface during sliding (Figure 9f). Similar brown tracks that belong to nickel oxide were reported in the literature, and these oxide layers were broken as the sliding distance increased (100 m) and the wear debris dispersed.[24] In this study, the sliding distance was 57.5 m. Therefore, only oxide layers were formed on the worn surface of the monolayer Ni–B coating, and the time was not provided to allow the oxide layers to dispersion. In the low-magnification image, the wear width of the duplex Ni–P/Ni–B coating was seen to be similar to that of the monolayer Ni–B coating (Figure 9d,g). In the high-magnification SEM image of the same coating, a severe delamination track was observed as a result of the wear test (Figure 9h). The wear debris was observed in large amounts on the $Al_2O_3$ ball compared to the monolayer Ni–B coating (Figure 9f,i). This result was compatible with the increase in the wear rate of the duplex Ni–P/Ni–B coating (Table 7). Micropores were observed in various parts of the worn surface in the high-magnification image of duplex Ni–B/Ni–P coatings, which showed a narrow wear width like other coatings (Figure 9j–k). In addition, dispersed and minor wear debris were found on the $Al_2O_3$ surface of the same duplex coating

 

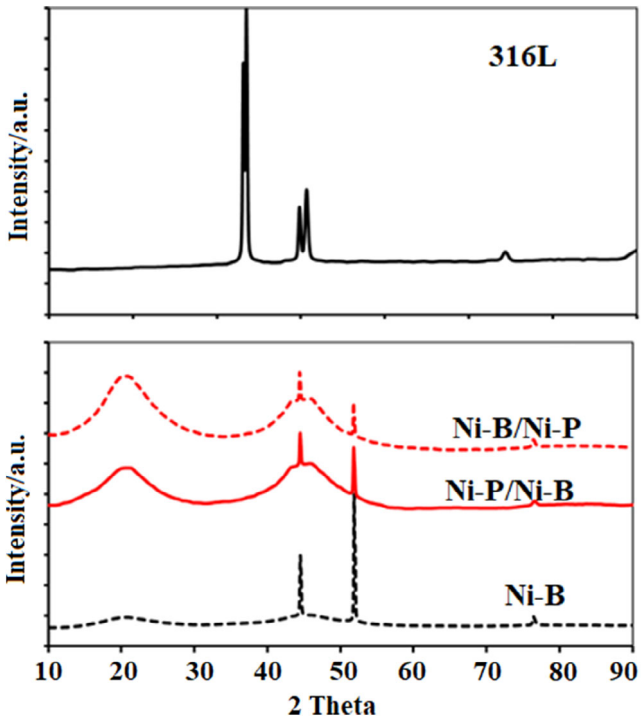


**Figure 6.** The XRD patterns of 316L and electroless coatings.

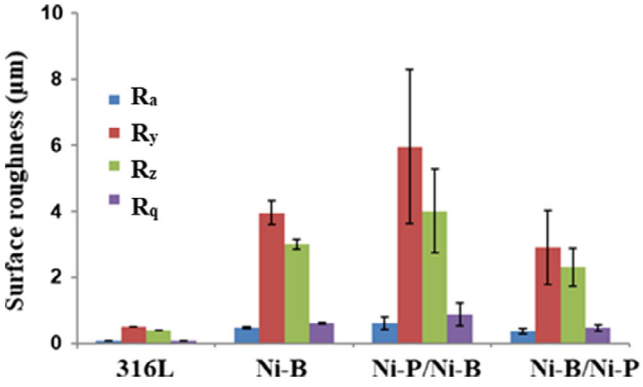


**Figure 7.** Surface roughness values of 316L and electroless coatings.

**Table 6.** Microhardness values of 316L and electroless coatings.

| Samples | Microhardness [$HV_{0.05}$] |
|---|---|
| 316L | 298 |
| DC | 337 |
| Ni–B | 686 |
| Ni–P/Ni–B | 616 |
| Ni–B/Ni–P | 480 |

(Figure 9I). According to the dry sliding wear test results, it was not expected that the wear resistance of the duplex Ni–B/Ni–P coating was higher than the duplex Ni–P/Ni–B coating. The presence of high wear-resistant Ni–B on the outer layer has been reported many times due to its high hardness and cauliflower-like microstructure.[12] However, in this study, duplex coating with Ni–P on the outer layer demonstrated better wear resistance. There were two different reasons for this result. The first reason was the microstructure of the duplex Ni–B/Ni–P coating, consisting of high-density, nonporous, and similarly sized spherical nodules. The second was the higher hardness and compressive strain of the Ni–B inner layer, which reduced the propagation of microcracks and the wear rate.[7] A schematic diagram of the wear mechanisms of 316L and electroless coatings is shown in Figure 9. The dry sliding wear results showed that the monolayer Ni–B coating and the duplex Ni–B/Ni–P coating had high resistance to plastic deformation, and the monolayer Ni–B coating also eliminated adhesion between the contact surfaces.

### 3.7. Electrochemical Corrosion Test

The electrochemical polarization curves of the 316L and coatings in 0.9% NaCl solutions at room temperature are shown in **Figure 10**a. The corrosion potential, corrosion current density, and corrosion rate of the samples obtained from the electrochemical polarization curves are summarized in **Table 8**. Both the monolayer Ni–B and the duplex Ni–P/Ni–B coatings showed great positive shifts in corrosion potential in comparison with its 316L substrate (Figure 10). As shown in Table 8, the duplex Ni–P/Ni–B coating had the most positive corrosion potential $E_{corr}$ (−248 mV) and the lowest corrosion current density $I_{corr}$ ($3.33 \times 10^{-6}$ A cm$^{-2}$) among the studied coatings. These results showed that the duplex Ni–P/Ni–B coating had the highest corrosion resistance. However, duplex Ni–B/Ni–P coating, which was expected to had the highest corrosion resistance, exhibited the most negative $E_{corr}$ value (−357 mV) and the highest $I_{corr}$ value ($17.3 \times 10^{-6}$ A cm$^{-2}$). The perfect corrosion resistance of the Ni–P coating was due to its amorphous structure, low surface porosity, and 11.0%P mass fraction.[11] The duplex Ni–B/Ni–P coating in this study had a compact and nonporous microstructure (Figure 4a–d), a mass fraction of 11.6% P (Table 6), and a semiamorphous structure (Figure 6). Therefore, it was expected to exhibit the best corrosion resistance. However, the reason for the high corrosion tendency was due to the formation of large cracks spreading over the entire surface, as can be seen from the corrosive surface image of the Ni–B/Ni–P coating in **Figure 11**. The corrosion rate values of all samples gave consistent results with $I_{corr}$ values (Table 8). Zhang et al.[37] reported that the corrosion resistance of the Ni–B/Ni–P coating was much higher than the Ni–B coating on AZ91D Mg alloy. They determined that the increase in the $I_{corr}$ value of the Ni–B coating was due to the fact that the microstructure of the coating was not compact and the penetration of the NaCl solution into the substrate through the micropores. In the literature, the reasons for the high $I_{cor}$ values of electroless Ni–P coatings are explained as follows: According to Zhang et al.,[31] the $Cl^-$ ions reacted with the Ni–P coating, causing local corrosion and coating destruction. Jasim et al.[34] explained the high corrosion rate because the semicrystalline structure of the Ni–P coating leads to a higher surface energy of the coating due to the accumulation of dislocations. Biswas et al.[17] demonstrated a heterogeneous surface with local variations in corrosion potential, which resulted in

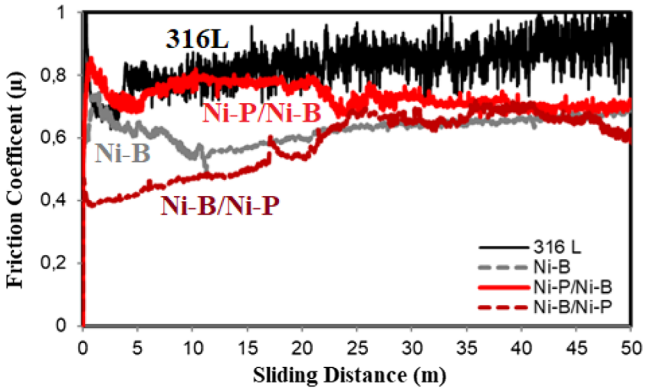


**Figure 8.** The friction coefficient profiles of the 316L and electroless coatings after dry sliding wear test.

**Table 7.** Wear volumes and wear rates of 316L and electroless coatings under dry sliding condition.

| Samples | Wear volume [$mm^3$] | Wear rate [$10^{-5} \times mm^3\ N^{-1}\ m^{-1}$] |
|---|---|---|
| 316L | 0.08 | 32 |
| Ni–B | 0.0005 | 0.2 |
| Ni–P/Ni–B | 0.006 | 2.4 |
| Ni–B/Ni–P | 0.00075 | 0.3 |

an intense attack by NaCl solution. In this study, cracks formed on the surface of the Ni–B/Ni–P coating did not reach the substrate material and therefore did not cause local corrosion of 316L. The Ni–B/Ni–P coating had the highest $I_{corr}$ value because the cauliflower-like spherical grain structure of the Ni–B inner layer caused a high electrochemical potential gap between Ni–B and Ni–P in the duplex coating layer, which results in a higher galvanic corrosion risk. Uppada et al.[38] reported similar corrosion results to Ni–P–$Al_2O_3$/Ni–P–SiC duplex coatings on a mild steel substrate. In this study, the Ni–B coating had a very compact microstructure with homogeneous grain size (Figure 2a–d) and outperformed the duplex Ni–B/Ni–P coating in corrosion resistance.

In Figure 10b, the OCP curves of 316L and its coatings were given for a period of 1800 s. It was reported that the higher the OCP, which thermodynamically reflects the corrosion resistance of a coating, the better is the corrosion resistance.[37] The results of the OCP curves in Figure 10b indicated that the duplex Ni–P/Ni–B and monolayer Ni–B coatings were more thermodynamically steady than 316L and duplex Ni–B/Ni–P coating in NaCl solution. The monolayer Ni–B and duplex Ni–P/Ni–B coating had a more compact structure than duplex Ni–B/Ni–P coating (Figure 2a–d, 3a–d, and 4a–d), which had better barrier performance against NaCl solution permeation. In addition, the monolayer Ni–B coating started to show more thermodynamically steady behavior after 900 s, and it indicated similar behavior with the duplex Ni–P/Ni–B coating after 1600 s. The polarization curves (Figure 10a) and electrochemical corrosion parameters (Table 8) of both coatings and the OCP results represented consistent results. The OCP of the duplex Ni–B/Ni–P coating was the lowest. The inertness of this coating was attributed to the cracks that appeared throughout the surface after corrosion (Figure 11).

SEM images of the 316L and coatings after the corrosion test were shown in Figure 11a–h. A small number of pit-shaped black pores were visible at the edges of the spherical nodule in low- and high-magnification images of monolayer Ni–B (Figure 11c,d) and duplex Ni–P/Ni–B coating (Figure 11e,f). Dark gray pits formed in large numbers and in different sizes on the corrosion surface of 316L (Figure 11a,b) and cracks formed throughout the corrosion surface of the duplex Ni–B/Ni–P coating were detected (Figure 11g,h). The corrosion behavior of 316L was consistent with the literature. It was reported in the literature that chloride solutions degraded the passive films on the surface of 316L and caused local corrosion, such as pitting.[39] The formation of black pores was attributed to the effectiveness of chloride, which degrades the passive films on the surface.[40] According to test results, duplex Ni–P/Ni–B and monolayer Ni–B coatings showed almost the same corrosion properties. As can be seen in Figure 10b, the high OCP potential of the duplex Ni–P/Ni–B duplex coating tended to decrease with the corrosive liquid that continued to penetrate into the small black pores (Figure 9h). The duplex Ni–P/Ni–B coating exhibited a lower potential between 1000 and 1600 s. than the monolayer Ni–B coating, which generally exhibited a stable potential. And the And the duplex Ni–P/Ni–B and monolayer Ni–B coatings showed almost the same potential values as each other after 1600 s. This result showed that the corrosive liquid did not penetrate under the Ni–B layer. If it had penetrated, the Ni–P layer, which is known to be more resistant to corrosion, would significantly increase the potential. As a result, it was understood that Ni–B layers showed superior resistance to corrosion before reaching the substrate in both coatings. Zhang et al.[11] reported the reasons for the use of Ni–B coating as an outer layer in duplex coatings in three ways. First, the Ni–B coating nucleated on defect areas on the Ni–P surface, and the Ni–B layer can prevent the corrosion solution from contacting the substrate. Second, the outer Ni–B layer with low corrosion potential corrodes the inner Ni–P layer with high corrosion potential. Third, the hard outer Ni–B layer provides excellent mechanical protection for the Ni–P inner layer. Therefore, it has been reported that the duplex Ni–P/Ni–B coating can provide better protection than the monolayer Ni–P or Ni–B coatings in practical application. In this study, it was determined that the duplex Ni–P/Ni–B coating had more corrosion resistance than the monolayer Ni–B coating. These results were attributed to the sealing of the Ni–B layer, which was the first way, and the high hardness of the Ni–B coating, which was the third way, to provide excellent mechanical protection. Vitry et al.[9a] reported that electroless Ni–P/Ni–B coating improved corrosion resistance due to its higher barrier efficiency than monolayer coatings, decreased the amount of porosity in cross-sectional images, and formed an interface that prevented the spread of deep pores during the coating process. According to the corrosion results of this study, it was determined that monolayer Ni–B and duplex Ni–P/Ni–B coatings showed almost similar behaviors.

 

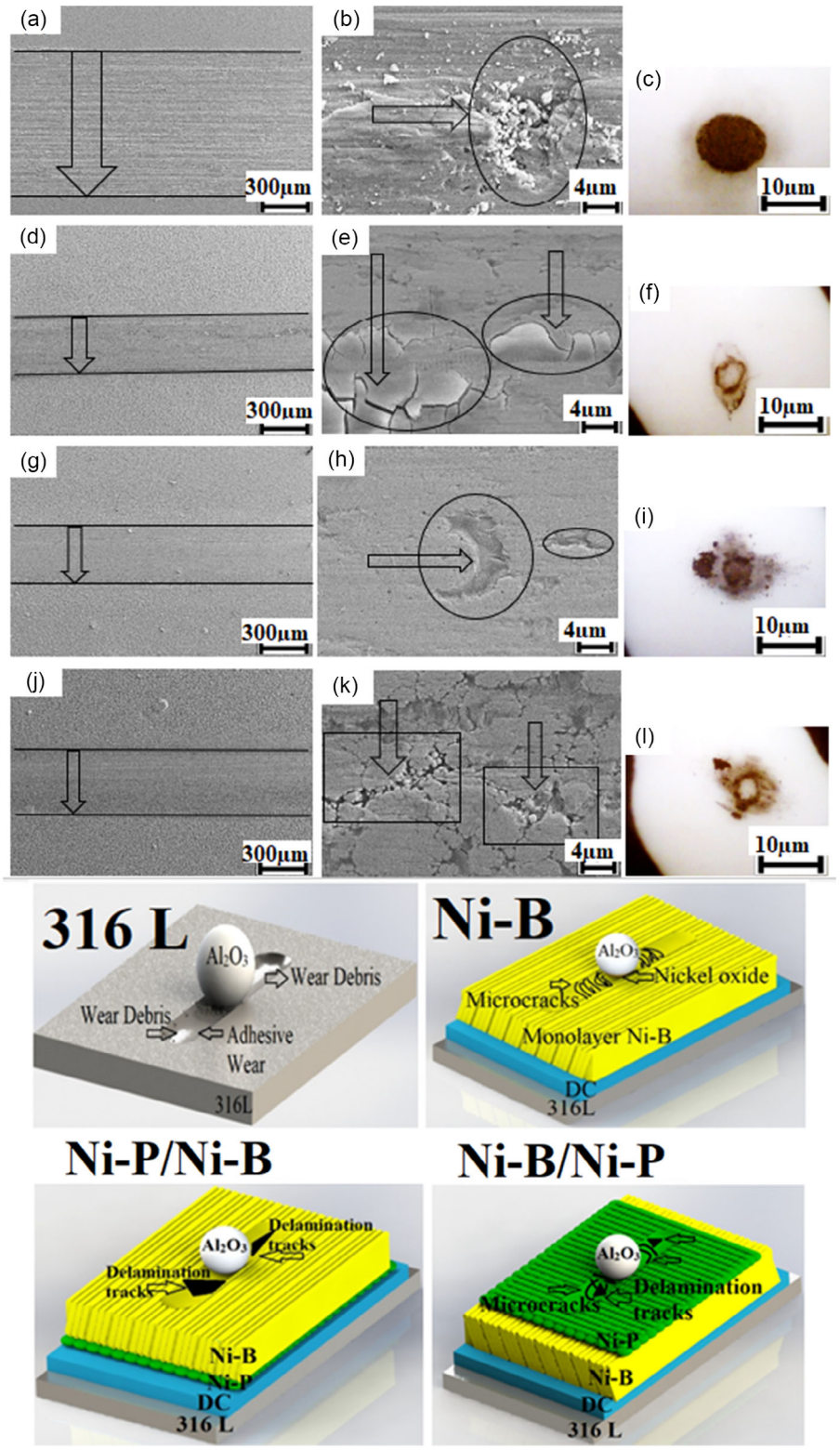


**Figure 9.** a,b) Low- and high-magnification SEM micrographs of wear tracks generated on the surface of the 316L, d–e) Ni–B, g,h) Ni–P/Ni–B, j,k) Ni–B/Ni–P coatings, and OM images of their corresponding testing balls, c,f,i,l) after dry sliding wear test and schematic views of the wear mechanisms of 316L and coatings utilized in this study.

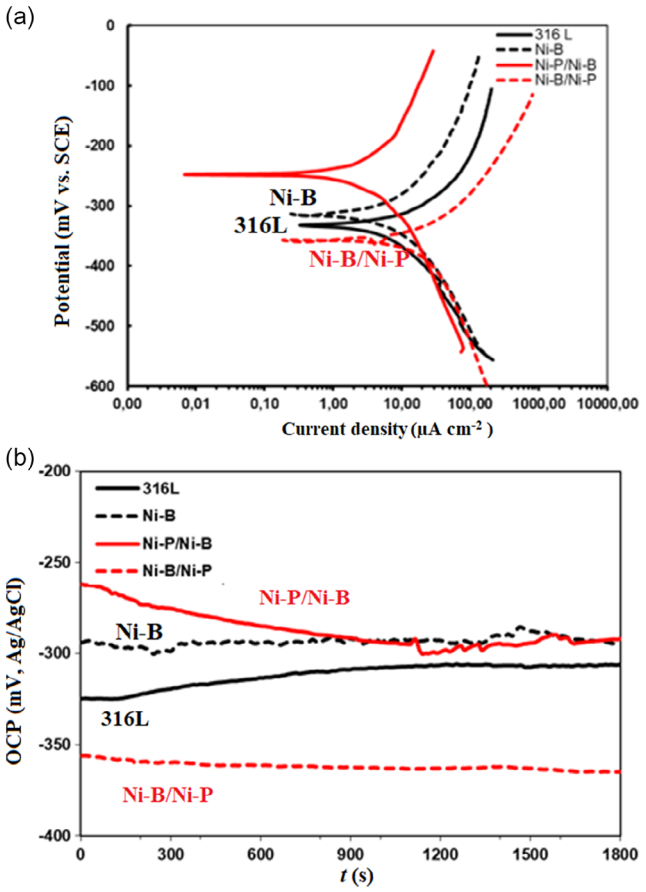


**Figure 10.** The a) electrochemical polarization and b) OCP curves of the 316L and coatings.

**Table 8.** The corrosion potential $E_{corr}$, corrosion current density $I_{corr}$, and corrosion rate of the samples.

| Samples | $E_{corr}$ [mV] | $I_{corr}$ [A cm$^{-2}$ ($\times 10^{-6}$)] | Corrosion rate [$\times 10^{-3}$ mm py] |
|---|---|---|---|
| 316L | −333 | 9.73 | 35.39 |
| Ni–B | −314 | 4.65 | 16.91 |
| Ni–P/Ni–B | −248 | 3.33 | 12.12 |
| Ni–B/Ni–P | −357 | 17.3 | 62.81 |

### 3.8. Tribocorrosion Test

Tribocorrosion tests were carried out under OCP conditions in a 0.9 wt% NaCl solution, and the potentials and the friction coefficient profiles of the coatings were evaluated. The OCP curves were given for the 316L and coatings in **Figure 12**. The OCP curves in Figure 12a were examined before the start of the test, during the test, and when the test was stopped. The OCP value of 316L was higher than all other coatings before the test started, and the OCP decreased rapidly from −180 to −390 mV after 600 s with the start of the test. A sudden drop occurred in potential with contact with the corrosive solution of the oxidation-prone surface.[41,42] At this potential value, the wear continued. Active surfaces became passive at the end of the test, and their potential increased with a tendency to reach the initial values. The tribocorrosion behavior of stainless steels was reported by Berradja et al.[43] They suggested that plastic deformation prevented the regeneration of the surface film and accelerated the dissolution of stainless steel. In the tribocorrosion test, monolayer Ni–B was the most thermodynamically stable coating, followed by Ni–P/Ni–B, and finally Ni–B/Ni–P coating. The potential decreased in the duplex Ni–P/Ni–B coating at the start of wear; this potential was much greater than that of monolayer Ni–B, and the duplex coating behaved close to a monolayer Ni–B coating, but it still had a lower potential during wear. After the test was stopped, the OCP values of all coatings did not return to the values at the beginning of the test. Among the coatings, the monolayer Ni–B coating had the closest value to the initial value. This indicates that it is caused by the corrosive liquid leaking from the cracks formed on the surface of the coating during wear.[44]

Figure 12b showed the friction coefficient profiles of 316L and coatings. All coatings had lower friction coefficient values than 316L. The average friction coefficient of 316L was 0.65, but the average friction coefficient values of Ni–B, Ni–P/Ni–B, and Ni–B/Ni–P coatings were found to be 0.43, 0.41, and 0.40, respectively. The monolayer Ni–B coating showed the most stable variation in the friction coefficient, but duplex coatings showed a decreasing trend depending on the sliding distance (Figure 12b). The friction coefficient values in the tribocorrosion test were lower than the dry sliding test results. This result was attributed to the lubricating effect of the liquid environment. However, in both test environments, the coatings gave close to each other's friction coefficient values, and these values were lower than the friction coefficient values of 316L. Therefore, it could be said that the reliability of the tests was ensured.

The wear volumes and wear rates of 316L and coatings after the tribocorrosion test in the 0.9 wt% NaCl solution are given in **Table 9**. SEM images of worn surfaces and OM images of corresponding $Al_2O_3$ balls are shown in **Figure 13**. As shown in Table 9, the wear volume and wear rate values of 316L were higher than all other coatings; this result could be observed by the wide wear width of the 316L in Figure 13a. In addition, the significant decrease in the OCP potential associated with the formation of the new active surface of 316L in Figure 12 had been reported in the literature as an indication that it will have a larger wear width.[44] In the tribocorrosion study of 316L in a 3.0 wt% NaCl solution reported by Dearnley and Aldrich-Smith,[45] it was observed that deep abrasive wear tracks and pits appeared in the worn surface of 316L. This image resembled the worn surface image of 316L in 0.9 wt% NaCl (Figure 13b). The $Al_2O_3$ ball was subjected to much more light wear because of the low hardness of the 316L (Figure 13c). The monolayer Ni–B coating with the lowest wear volume and wear rate values (Table 9) had the smallest wear track width among other samples (Figure 13d). In the tribocorrosion condition, the wear rates of Ni–B, Ni–P/Ni–B, and Ni–B/Ni–P coatings were reduced by 98.5%, 30.1%, and 19.1%, respectively, when compared to 316L (Table 9). Pits of varying sizes were clearly visible in the worn surface of the monolayer Ni–B coating (Figure 13e) and a negligible amount of material transfer was observed on the $Al_2O_3$ ball (Figure 13f). In the high-magnification SEM image of the Ni–P/Ni–B duplex coating, which

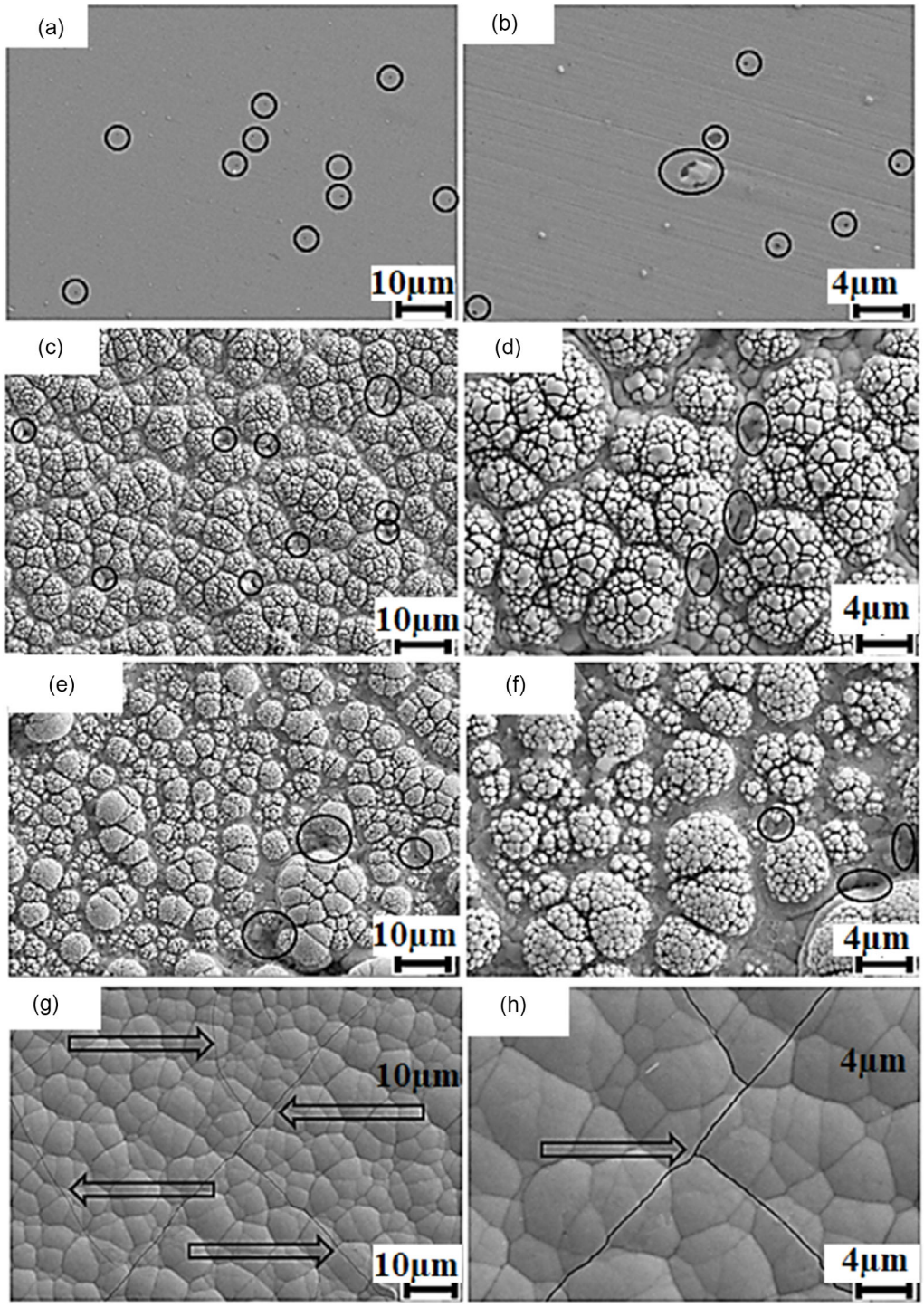


**Figure 11.** a,b) Low- and high-magnification SEM micrographs of the 316L, c,d) Ni–B, e,f) Ni–P/Ni–B, and g,h) Ni–B/Ni–P coatings after corrosion test.

exhibited higher tribocorrosion performance than the duplex Ni–B/Ni–P coating, there were deeper and wider tracks on the worn surface (Figure 13h). The contact surface of the mating $Al_2O_3$ ball revealed the material transfer from the Ni–P/Ni–B duplex coating to the periphery of the contact surface of the $Al_2O_3$ ball (Figure 13i). On the other hand, rubbing of $Al_2O_3$ ball caused abrasive and plastic deformation damage on the duplex Ni–B/Ni–P coating (Figure 13j,k). The size of the wear scar formed on the contact surface of $Al_2O_3$ ball was lower than monolayer Ni–B and Ni–P/Ni–B duplex coatings (Figure 13I). It was understood that there were not very large and bulky wear debris in all coatings; these debris did not act as a two-to-three body, and

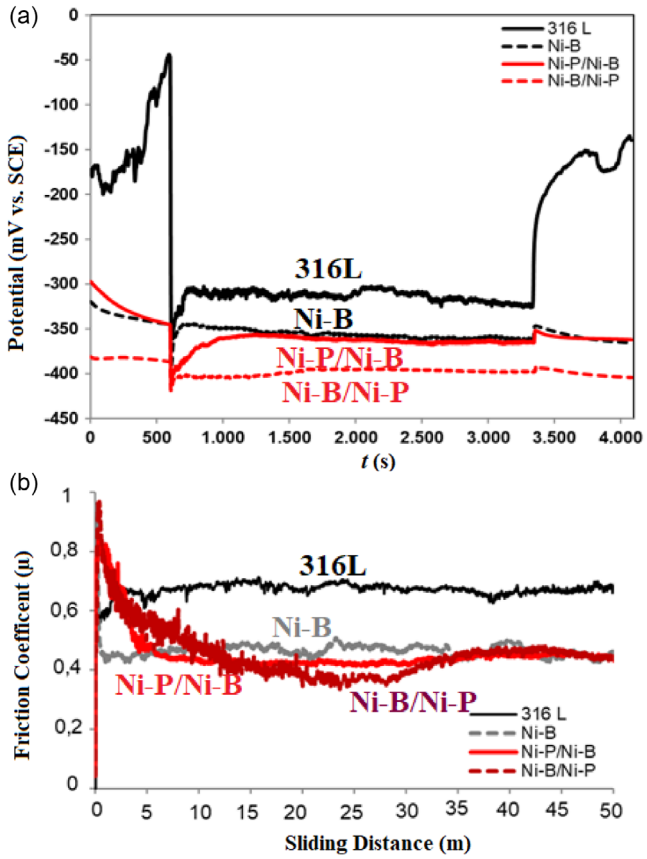


**Figure 12.** The a) OCP curves and b) friction coefficient profiles of 316L and coatings after tribocorrosion test.

**Table 9.** The wear volume and wear rate values of 316L and coatings.

| Samples | Wear volume [$mm^3$] | Wear rate [$10^{-5} \times mm^3 N^{-1} m^{-1}$] |
|---|---|---|
| 316L | 0.017 | 6.8 |
| Ni–B | 0.00025 | 0.1 |
| Ni–P/Ni–B | 0.0118 | 4.75 |
| Ni–B/Ni–P | 0.01375 | 5.5 |

they did not cause an increase in the friction coefficient values of the coatings.[46] Schematic views of the wear mechanisms of 316L and coatings in tribocorrosion conditions are shown in Figure 13.

### 3.9. Contact Angle Tests

**Figure 14** shows the water contact angles of 316L and its coatings. Experimental results indicated that all coatings had a high contact angle compared with 316L (Figure 14). Duplex coatings exhibited similar contact angles around 111° and 102°, which meant they were both hydrophobic. The monolayer Ni–B coating had the highest hydrophobicity, at around 132°. Wang et al.[47] reported that it was important to protect the hydrophobicity of the coating surface without sacrificing other properties. Other results of this study demonstrated the usability of a monolayer Ni–B coating instead of duplex coatings. Its high hydrophobicity also contributed to other properties. The monolayer Ni–B coating with a high contact angle (132°) indicates that the coating surface has better hydrophobicity. It is concluded that the presence of the corrosion solution prevented direct contact between the coating and the $Al_2O_3$ ball due to the good hydrophobic property of the monolayer Ni–B coating. The superior improvement in the wear resistance of the monolayer Ni–B coating in dry sliding and corrosive conditions was attributed to its compact structure with more homogeneous nodules (Figure 2) and high hardness values, as well as an increase in the hydrophobic role of the Ni–B coating during wear testing.

### 3.10. The Electrical Conductivity Test

The electrical conductivity values of the 316L and coatings are shown in **Table 10**. The electrical conductivity values of 316L and duplex Ni–B/Ni–P coating were similar. This result showed that the duplex Ni–B/Ni–P coating could not act as a protective barrier between the metal and its environment. The cracks that formed on the surface of the same coating after corrosion also supported this result (Figure 11g,h). Comparing the 316L and the duplex Ni–B/Ni–P coating, the duplex Ni–P/Ni–B (Ni–P as an inner layer and Ni–B as the outer layer of deposition) coating had the highest conductivity value. The tunneling resistant and contact resistance of the duplex coating decreased because the interface between two coatings did not act as insulated layer due to the formation of spherical nodules of varying sizes (Figure 3a–g). As shown in Table 10, the monolayer Ni–B coating had much lower electrical conductivity than duplex coatings and 316L. Song et al.[48] reported that noble metals such as gold, silver, and palladium and passive metals such as tin and nickel are used to form protective surfaces for the corrosion protection of electrically conductive surfaces. The high OCP value (Figure 12a) of the monolayer Ni–B coating under tribocorrosion conditions could be attributed to its low conductivity, excellent corrosion and wear resistance among the coatings.

## 4. Conclusions

In this study, monolayer Ni–B and duplex Ni–P/Ni–B and Ni–B/Ni–P coatings were formed by the electroless coating method. Monolayer Ni–B and duplex Ni–P/Ni–B coatings presented a typical cauliflower-like structure with spherical grains. The duplex Ni–B/Ni–P coating showed characteristically uniform spherical nodules. XRD analysis revealed that the coatings were a hybrid structure of crystalline and amorphous. According to the electrochemical test, the duplex Ni–P/Ni–B coating had the most positive corrosion potential $E_{corr}$ (−248 mV) and the lowest corrosion current density $I_{corr}$ ($3.33 \times 10^{-6}$ A $cm^{-2}$) among all the coatings. Monolayer Ni–B coating exhibited superior hardness, high wear resistance, good hydrophobicity, and low electrical conductivity relative to the 316L and duplex coatings. The monolayer Ni–B coating exhibited the highest hardness and showed excellent wear resistance in both dry sliding and tribocorrosion conditions.

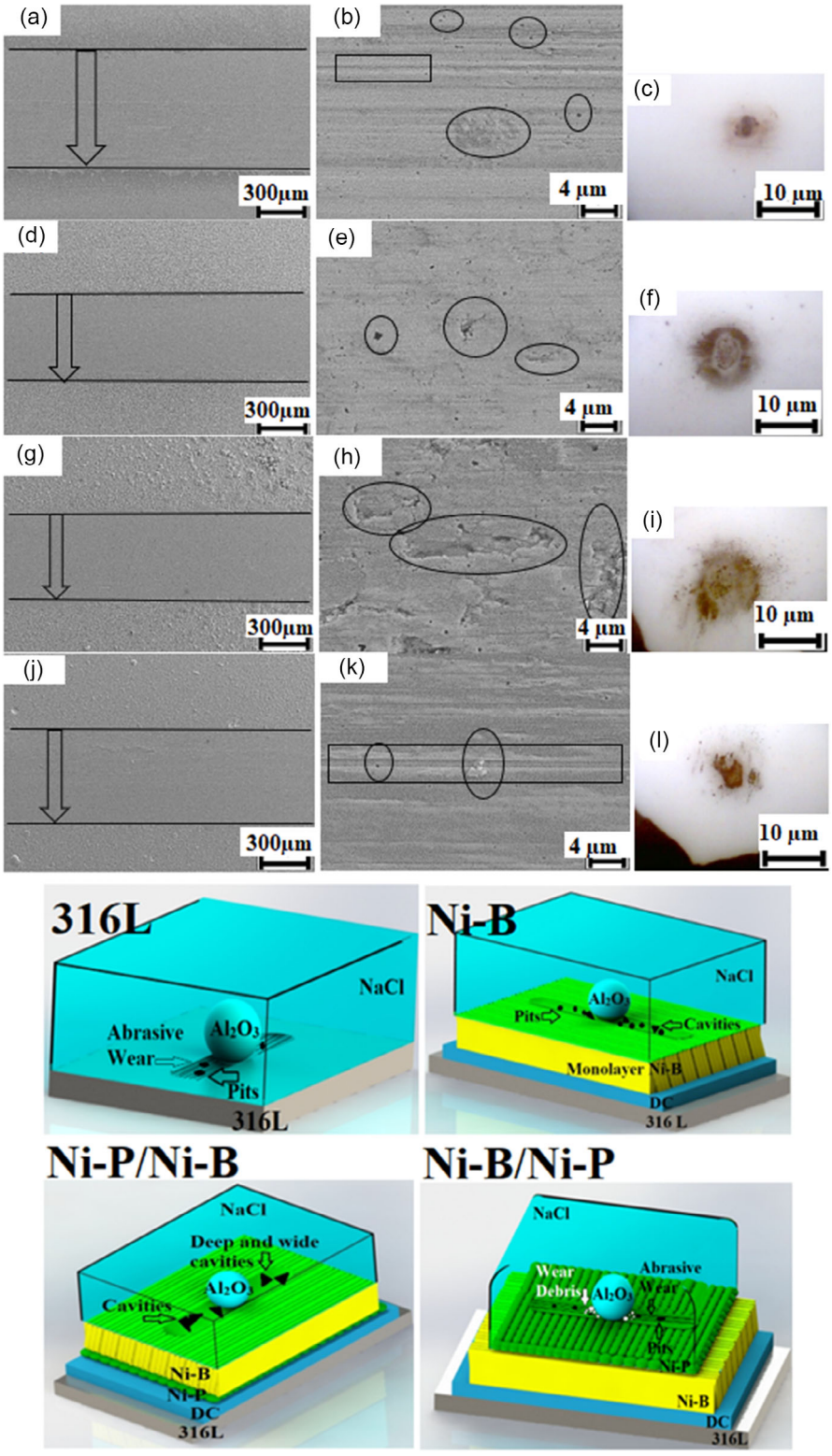


**Figure 13.** a,b) Low- and high-magnification SEM micrographs of wear tracks generated on the surface of the 316L, d,e) Ni–B, g,h) Ni–P/Ni–B, and j,k) Ni–B/Ni–P coatings, and OM images of their corresponding testing balls c,f,i,l) after tribocorrosion test and schematic views of the tribocorrosion mechanisms of 316L and coatings utilized in this study.

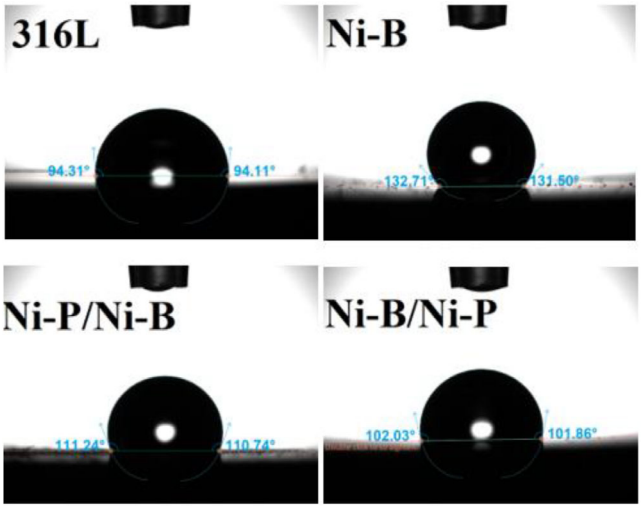


**Figure 14.** Water contact angles of 316L and coatings.

**Table 10.** The electrical conductivity of the 316L and coatings.

| Samples | Electrical conductivity [S $m^{-1}$] |
|---|---|
| 316L | 8.600374976 |
| Ni–B | 0.020106651 |
| Ni–P/Ni–B | 14.24014582 |
| Ni–B/Ni–P | 8.383283732 |

## Acknowledgements

The authors gratefully acknowledge the support of the Surface Research Laboratory for the equipment supplied to the Mechanical Engineering Department of Bilecik Şeyh Edebali University, which was utilized in this study.

## Conflict of Interest

The authors declare no conflict of interest.

## Data Availability Statement

The data that support the findings of this study are available from the corresponding author upon reasonable request.

## Keywords

AISI 316L, dry sliding wear, electroless coating, electrolytic corrosion, tribocorrosion

Received: October 17, 2022
Revised: February 17, 2023
Published online: March 17, 2023

[1] R. C. Agarwala, V. Agarwala, *Sadhana* **2003**, *28,* 475.
[2] M. Ocal, Ph.D. Thesis, Atatürk University, **2020**.
[3] F. Bülbül, H. Altun, V. Ezirmik, O. Küçük, *Proc. IMechE Part J: J. Eng. Tribol.* **2013**, *227*, 629.
[4] C. A. Loto, *Silicon* **2016**, *8,* 177.
[5] J. Sudagar, J. Lian, W. Sha, *J. Alloys Compd.* **2013**, *571*, 183.
[6] G. Dil, A. Göksenli, Ç. Calli, F. Muhaffel, A. I. Aydeniz, A. Yıldız, B. Yüksel, *Adv. Mater. Res.* **2014**, *853,* 264.
[7] A. Tohidi, S. M. Monirvaghefi, A. Hadipour, *T. Indian I. Metals* **2017**, *70*, 1735.
[8] J. Zhang, Z.-H. Xie, H. Chen, C. Hu, L. Li, B. Hu, Z. Song, D. Yan, G. Yu, *Surf. Coat. Technol.* **2018**, *342,* 178.
[9] a) V. Vitry, A. Sens, A.-F. Kanta, F. Delaunois, *Surf. Coat. Technol.* **2012**, *206*, 3421; b) V. Vitry, A.-F. Kanta, F. Delaunois, *Mater. Des.* **2012**, *39*, 269.
[10] W. X. Zhang, Z. H. Jiang, G. Y. Li, Q. Jiang, J. S. Lian, *Appl. Surf. Sci.* **2008**, *254,* 4949.
[11] J. Zhang, Z. Song, G. Yu, B. Hu, X. Zhang, *Int. J. Electrochem. Sci.* **2016**, *11*, 10053.
[12] T. S. N. Narayanan Sankara, K. Krishnaveni, S. K. Seshadri, *Mater. Chem. Phys.* **2003**, *82*, 771.
[13] A. Baibordi, M. H. Bina, K. Amini, A. Dehghan, *Int. J. ISSI* **2012**, *9*, 1.
[14] V. Vitry, L. Bonin, L. Malet, *Surf. Eng.* **2017**, *34*, 475.
[15] Q. Zhao, C. Liu, X. Su, S. Zhang, W. Song, S. Wang, G. Ning, J. Ye, Y. Lin, W. Gong, *Appl. Surf. Sci.* **2013**, *274*, 101.
[16] H. Wu, Z. Luo, Y. Dong, L. Yao, R. Song, Y. Xu, *Surf. Coat. Technol.* **2022**, *443*, 128637.
[17] P. Biswas, S. K. Das, P. Sahoo, *J. Electrochem. Sci.* **2022**, *12*, 1261.
[18] S. Kundu, S. K. Das, P. Sahoo, in *Advances in Materials, Mechanical and Industrial Engineering*, Springer, Cham **2019**.
[19] Z. Rajabalizadeh, D. Seifzadeh, A. Khodayari, S. Sohrabnezhad, *J. Magnes. Alloys* **2022**, *10*, 2280.
[20] Z. Song, Z. Xie, L. Ding, Y. Zhang, X. Hu, *Colloids Surf. A Physicochem. Eng. Asp.* **2022**, *632*, 127699.
[21] J. G. Castaño, S. Arias, O. Galvis, *Corros. Eng. Sci. Technol.* **2020**, *55*, 83.
[22] F. Zouch, Z. Antar, A. Bahri, K. Elleuch, M. Ürgen, *J. Tribol.* **2018**, *140*, 011301.
[23] F. Mindivan, *M.Sc. Thesis*, Bursa Uludağ University, **2021**.
[24] F. Madah, C. Dehghanian, A. A. Amadeh, *Surf. Coat. Technol.* **2015**, *282*, 6.
[25] U. Matik, *Kovove Mater.* **2020**, *58*, 247.
[26] M. Dadfar, M. H. Fathi, F. Karimzadeh, M. R. Dadfar, A. Saatchi, *Mater. Lett.* **2007**, *61*, 2343.
[27] I. Baskaran, R. S. Kumar, T. S. N. Sankara Narayanan, A. Stephen, *Surf. Coat. Technol.* **2006**, *200*, 6888.
[28] M. Czagány, P. Baumli, G. Kaptay. *Appl. Surf. Sci.* **2017**, *423*, 160.
[29] K. Krishnaveni, T. S. N. N. Sankara, S. K. Seshadri, *Surf. Coat. Technol.* **2005**, *190*, 115.
[30] M. Barman, T. K. Barman, P. Sahoo, *Proc. Inst. Mech. Eng. C J. Mech. Eng. Sci.* **2023**, *237*, 183.
[31] Z. Zhang, Y. He, Y. Bai, R. Song, Y. He, B. Liu, J. Shangguan, *Colloids Surf. A Physicochem. Eng. Asp.* **2022**, *655*, 130100.
[32] A. Mukhopadhyay, T. K. Barman, P. Sahoo, *Surf. Coat. Technol.* **2017**, *321*, 464.
[33] V. Nemane, V. Sharma, S. Chatterjee, *J. Tribol.* **2022**, *144*, 121401.
[34] A. H. Jasim, A. R. K. Abidali, A. M. H. Wais, *Mater. Sci.* **2023**.
[35] I. Saravanan, A. Elaya Perumal, S. C. Vettivel, N. Selvakumar, A. Baradeswaran, *Mater. Des.* **2015**, *67*, 469.
[36] G.-J. Li, J. Wang, C. Li, Q. Peng, J. Gao, B.-I. Shen, *Nucl. Instrum. Methods Phys. Res., B* **2008**, *266*, 1964.
[37] J. Zhang, Z.-H. Xie, H. Chen, C. Hu, L. Li, B. Hu, Z. Song, D. Yan, G. Yu, *Surf. Coat. Technol.* **2018**, *342*, 178.
[38] S. Uppada, R. Koona, V. B. Chintada, R. Koutavarapu, *Silicon* **2022**, 1.
[39] B. Cai, Y. Liu, X. Tian, F. Wang, H. Li, R. Ji, *Corros. Sci.* **2010**, *52*, 3235.

[40] M. Crobu, A. Scorciapino, B. Elsener, A. Rossi, *Electrochim. Acta* **2008**, *53*, 3364.
[41] M. Azzi, M. Paquette, J. A. Szpunar, J. E. Klemberg-Sapieha, L. Martinu, *Wear* **2009**, *267*, 860.
[42] P. Ponthiaux, F. Wenger, D. Drees, J.-P. Celis, *Wear*, **2004**, *256*, 459.
[43] A. Berradja, F. Bratu, L. Benea, G. Willems, J.-P. Celis, *Wear* **2006**, *261*, 987.
[44] R. Offoiach, M. Lekka, A. Lanzutti, L. Fedrizzi, V. Martínez-Nogués, J. M. Vega, E. García-Lecina, *Surf. Coat. Technol.* **2019**, *369*, 1.
[45] P. A. Dearnley, G. Aldrich-Smith, *Wear* **2004**, *256*, 491.
[46] B. A. Obadele, M. L. Lepule, A. Andrews, P. A. Olubambi, *Tribol. Int.* **2014**, *78*, 160.
[47] Y. Wang, X. Shu, S. Wei, C. Liu, W. Gao, R. A. Shakoor, R. Kahraman, *J. Alloys Compd*. **2015**, *630*, 189.
[48] J. Song, L. Wang, A. Zibart, C. Koch, *Metals* **2012**, *2*, 450.